Ultrasonically Encoded Photoacoustic Flowgraphy in Biological Tissue

Lidai Wang, Jun Xia, Junjie Yao, Konstantin I. Maslov, and Lihong V. Wang*

*Department of Biomedical Engineering, Optical Imaging Laboratory, Washington University in Saint Louis Campus Box 1097,
One Brookings Drive, Saint Louis, Missouri 63130-4899, USA*

Blood flow speed is an important functional parameter. Doppler ultrasound flowmetry lacks sufficient sensitivity to slow blood flow (several to tens of millimeters per second) in deep tissue. To address this challenge, we developed ultrasonically encoded photoacoustic flowgraphy combining ultrasonic thermal tagging with photoacoustic imaging. Focused ultrasound generates a confined heat source in acoustically absorptive fluid. Thermal waves propagate with the flow and are directly visualized in pseudo color using photoacoustic computed tomography. The Doppler shift is employed to calculate the flow speed. This method requires only acoustic and optical absorption, and thus is applicable to continuous fluid. A blood flow speed as low as $0.24 \text{ mm} \cdot \text{s}^{-1}$ was successfully measured. Deep blood flow imaging was experimentally demonstrated under 5-mm-thick chicken breast tissue.

High-resolution blood flow imaging in deep tissue offers valuable functional information for diagnosing and assessing many diseases [1–4]. Doppler ultrasound is a longstanding technology that achieves high-resolution noninvasive flow imaging at depths [1]. However, Doppler ultrasound suffers from two major limitations. The first is the poor sensitivity to blood [2]. The Doppler signal relies on ultrasound scattering from flowing blood cells, which is usually much weaker than the scattering from surrounding tissues. Since ultrasound attenuates exponentially with its frequency and propagation path length, low frequency ultrasound is often used to measure blood flow in deep tissue, which weakens scattering even further. The second limitation is that slowly flowing blood cells cause small Doppler shifts, which are difficult to separate from Doppler signals due to surrounding tissues. These limitations make Doppler ultrasound difficult to measure slow flow without contrast agents [2,5,6]. A new technique that can measure slow blood flow should find many biomedical applications, such as functional brain imaging, early cancer detection, and treatment monitoring, and the detection of intraluminal atherosclerotic plaques.

In comparison, photoacoustic (PA) tomography has recently been recognized as a promising technique enabling high-resolution deep *in vivo* imaging [7–13]. PA imaging provides unique optical absorption contrast beyond the ballistic regime, as well as high sensitivity to blood in the visible and near-infrared spectral range. PA measurement of blood flow has attracted growing interest [14–20]. In the ballistic and quasiballistic regimes (~1 mm deep in soft tissue), an optical beam can be effectively focused, allowing for sensing cellular-level features and then readily computing the flow speed. However, in the quasidiffusive and diffusive regimes, fine features cannot be well resolved. Unlike ultrasound, PA signals tend to have weak speckles and strong boundaries

[21,22], precluding Doppler sensing in continuously absorbing flow. Although time-domain cross correlation and frequency-domain Doppler shift have been demonstrated on blood mimicking phantoms [14,17,19], neither method succeeded in whole blood flow sensing, due to the high density of blood cells. Therefore, high-resolution PA blood flow sensing in deep tissue remains a challenge.

To overcome these challenges in Doppler ultrasound and PA flow sensing, we developed ultrasonically encoded photoacoustic flowgraphy (UE-PAF) for slow blood flow imaging in deep tissue. In UE-PAF, sinusoidally modulated ultrasound is focused into the flowing medium to generate confined heat sources due to acoustic absorption. PA computed tomography is then utilized to image the heat propagation in the fluid, with optical absorption contrast and photoacoustically determined spatial resolution. Since optical absorption is usually orders of magnitude stronger in blood than in surrounding tissues in the visible and near-infrared spectral range, PA imaging of blood provides higher contrast than ultrasound imaging. The PA signal is sensitive to temperature; thus, the heat propagation can be clearly imaged in flowing blood. In addition, as the heat source is modulated at a given frequency, its signal can be easily separated from the motion signal of surrounding tissues.

Method.—We assume that the ultrasonic heating is fixed at $x = 0$, the flow speed is v_f, the angle between the flow vector and the x axis is θ, and thermal conduction is negligible during PA imaging. The fluid temperature in response to sinusoidal heating varies according to

$$\tilde{T}(t, x) = A_T(x) \sin\left[2\pi f_0 \left(t - t_0 - \frac{x}{v_f \cos\theta} \right) \right], \quad (1)$$

where $\tilde{T}$ is the temperature variation from the average temperature, t is the "slow" time instead of the "fast" PA flight time, A_T is the amplitude of the temperature

variation at x, f_0 is the heating modulation frequency, and t_0 is a constant. We have $A_T(x) = A_T(0) \times \exp[-(\alpha\beta/v_f \cos(\theta))x]$, where $A_T(0)$ is a constant, α is the thermal diffusivity, and β is a constant coefficient. The detailed derivation of $A_T(x)$ can be obtained in the Supplemental Material [23].

The temperature variation refers to the slowly changing temperature induced by ultrasonic heating, rather than the instantaneous temperature rise induced by pulsed optical absorption. The "slow" time refers to the sub-second-scale PA measurement time at each laser pulse, and the "fast" time is the microsecond-scale photoacoustic flight time within each PA measurement.

In PA imaging, if the optical excitation is in both thermal and stress confinements, the initial pressure p_0 can be approximated as a linear function of temperature [12,24–26] as

$$p_0(t, x) = [a + bT_0 + b\tilde{T}(t, x)]\mu_a(x)F(x), \quad (2)$$

where p_0 denotes the magnitude of the initial pressure induced by each laser pulse, a and b are empirical constants, T_0 is the average temperature, μ_a is the optical absorption coefficient, and F is the optical fluence. We assume that T_0, μ_a, and F are time invariant. The time-variant part of the pressure magnitude $\tilde{p}_0$ can be written as

$$\tilde{p}_0(t, x) = A_p(x)\sin\left\{2\pi f_0\left[t - t_0 - \frac{x}{v_f \cos(\theta)}\right]\right\}, \quad (3)$$

where $A_p(x) = b\mu_a(x)F(x)A_T(0)\exp[-(\alpha\beta/v_f \cos(\theta))x]$.

If we measure the pressure point by point, and linearly scan the measurement point along the flow direction at a speed of v_m, then we have $x = v_m t$. Equation (3) then becomes

$$\tilde{p}_0(t) = A_p(v_m t)\sin\left\{2\pi f_0 t\left[1 - \frac{v_m}{v_f \cos(\theta)}\right] - 2\pi f_0 t_0\right\}. \quad (4)$$

If the amplitude $A_p(v_m t)$ varies slowly, then $\tilde{p}_0(t)$ can be separated through envelope detection into an amplitude modulation signal $A_p(v_m t)$ and a sinusoidal carrier signal $\sin\{2\pi f_0 t[1 - (v_m/v_f \cos(\theta))] - 2\pi f_0 t_0\}$. The Doppler shift of the carrier signal from the heating frequency is

$$\Delta f = -\frac{v_m}{v_f \cos(\theta)}f_0. \quad (5)$$

When $v_m = v_f \cos(\theta)$, the Doppler shift will reduce the carrier signal to a constant of $\sin(-2\pi f_0 t_0)$.

In reality, it is difficult to always scan the detection point at the same speed as the blood flow. Instead, we can first acquire a series of two-dimensional (2D) PA images and then resample the PA signals at different positions with a certain time interval during postprocessing. The artificial scanning speed can be changed by tuning the spatial and temporal step sizes. When the carrier signal of $\tilde{p}(t)$ varies

minimally, the tuned scanning speed is equal to the flow speed.

With a 2D imaging capability, the phase shift between different positions can also be used to determine the flow speed $v_f \cos(\theta)$. From Eq. (3), at positions x_1 and $x_1 + \Delta x$, the phases of the carrier signals are $\phi_1 = -2\pi f_0(x_1/v_f \cos(\theta))$ and $\phi_2 = -2\pi f_0(x_1 + \Delta x/v_f \cos(\theta))$, respectively. The phase shift is $\Delta\phi = -2\pi f_0(\Delta x/v_f \cos(\theta))$. Simultaneous measurements of $\tilde{p}_0(t, x_1)$ and $\tilde{p}_0(t, x_1 + \Delta x)$ give the phase shift of $\Delta\phi$. With known f_0 and Δx, the flow speed $v_f \cos(\theta)$ can be readily determined. Similarly, flow speed can also be calculated from cross correlation between two consecutive 2D images. These two methods are equivalent to the above Doppler shift method.

Figure 1(a) shows a schematic of the UE-PAF system used in experiments. A single-element focused ultrasound transducer is used to sinusoidally heat up a fixed confined volume of blood. The heat propagates with blood flow, generating a temperature gradient along the blood flow direction. At the same time, nanosecond laser pulses are delivered to the blood, inducing PA signals. The laser beam is expanded so that absorbers over a large area are excited simultaneously. A ring-shaped receiving ultrasound transducer array is used to detect the PA waves propagating in different directions. The received PA signals are then reconstructed using backprojection [27] to form two-dimensional images. The value of each pixel is proportional to its local initial pressure rise, which is linearly related to the local temperature. Detailed description of the experimental setup can be found in the Supplemental Material [23].

Taking advantage of the full-ring receiving aperture, we can set the reconstruction x axis along the flow direction, so that the angle θ is zero and the measured flow speed is v_f. It should be noted that in general cases, the measured flow speed is $v_f \cos(\theta)$.
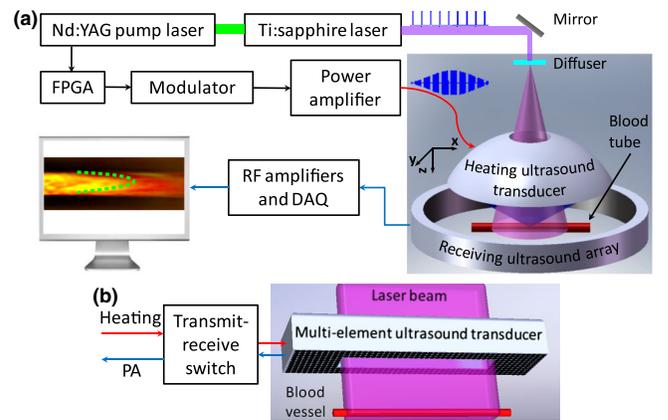

FIG. 1 (color online). Experimental setup. (a) Schematic of an ultrasonically encoded photoacoustic flowgraphy (UE-PAF) system. (b) Conceptual design of a reflection-mode UE-PAF probe.

The heating ultrasound transducer is concave with a hole in the center for light delivery. The central frequency and radius for the heating transducer are 7.5 MHz and 24 mm, respectively. The effective heating spot within the blood tube has a diameter of $\sim$1 mm. The average power of the heating ultrasound is adjusted between 2 and 5 W, so that temperature modulation can be observed in the PA signals. The average ultrasound intensity in the blood tube is estimated to be less than 500 W $\cdot$ cm^{-2}.

The current experimental setup, shown in Fig. 1(a), was developed to demonstrate the principles. For future clinical practices, reflection-mode UE-PAF can be developed, allowing easy access to different anatomical sites. Figure 1(b) shows a conceptual design of a reflection-mode UE-PAF probe. A two-dimensional ultrasound transducer array is used to dynamically focus the heating. The array has an opening in the center, so that an expanded laser beam can pass through. The ultrasound array is also used to receive PA signals. A transmit-receive switch is employed to alternate the ultrasound array between the heating and PA detection modes.

Results and discussions.—Reconstructed PA images were first averaged over all frames in several heating cycles, so that a stable background image could be obtained without the thermally induced fluctuations. Then the background image was subtracted from each subsequent PA image, producing a relative temperature change map of the blood, i.e., the $b\tilde{T}(t, x)\mu_a(x)F(x)$ term in Eq. (2). The temperature map was color coded to show the changes from the average temperature. Figure 2(a) shows a typical photoacoustic image of whole blood without ultrasonically encoding, where no features can be resolved for flow sensing. Figures 2(b)–2(g) present six consecutive images showing the PA signal variations due to heat propagation in flowing whole blood. The heating spot is centered at the middle point of the left edge. Blood flows towards the positive x axis. Parabolic thermal waves can be visualized as they propagate downstream. Supplemental Material, video 1 [23] shows a movie of the thermal wave propagating in blood flow. To increase the

signal-to-noise ratio, the PA changes were averaged over multiple consecutive heating cycles.

To measure the flow speed, PA flow images were converted into thermal flow trajectories in a spatiotemporal (x-t) plane. As illustrated in Fig. 3, for each flow image, one line along the flow path was extracted. Lines from consecutive frames were placed together to form the temporal dimension. The trajectories in the x-t plane were resampled along the direction of $x = v_m t$. By adjusting the slope v_m, we can determine the flow speed when the resampled data reach the minimum variation.

Figures 4(a)–4(c) show three representative thermal trajectory images at different flow speeds. As expected, the steepness of the trajectory on the x-t plane becomes smaller when flow speed increases. The slopes of the thermal trajectories ($\Delta x/\Delta t$) were determined by local peak detection on the x-t plane, followed by linear fitting. A coefficient that converts the trajectory slopes to flow speeds was calibrated by measuring a known blood flow speed. Different flow speeds were set from 0.24 to 11.80 mm $\cdot$ s^{-1} using a syringe pump. The measured flow speed was plotted in Fig. 4(d). The measurement error was estimated with the normalized root-mean-square deviation, which were 2.7%, respectively.

In a blood phantom, we experimentally measured a flow speed as low as 0.24 $\pm$ 0.01 mm $\cdot$ s^{-1}, which was less than one fourth of the lowest speed detectable by Doppler ultrasound flowmetry [5]. The limiting factors on slow-flow detection are thermal diffusion, the heating spot size, and the signal-to-noise ratio. According to Eq. (3), the slowest detectable flow has to be fast enough so that the fluid can travel through the heating region before the thermal diffusion smoothes the modulated temperature distribution below the noise level. In future studies, the lowest detectable flow speed can be further reduced by optimizing the heating spot size.
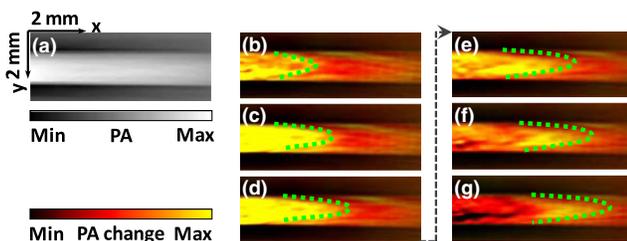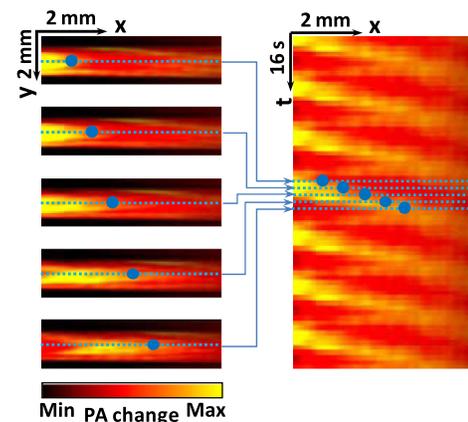

FIG. 2 (color online). (a), A typical photoacoustic image of blood flow without ultrasonically encoding. (b)–(g), Ultrasonically encoded photoacoustic flow images of whole blood in a tube. Time interval between adjacent images is 1.6 sec. Dashed line highlights a parabolic heating peak propagating with blood flow.

FIG. 3 (color online). Flow trajectories in the x-t plane. Each horizontal line in the right figure is extracted from one photoacoustic image along the flow direction. The blue dots represent a trajectory of a thermally tagged feature.
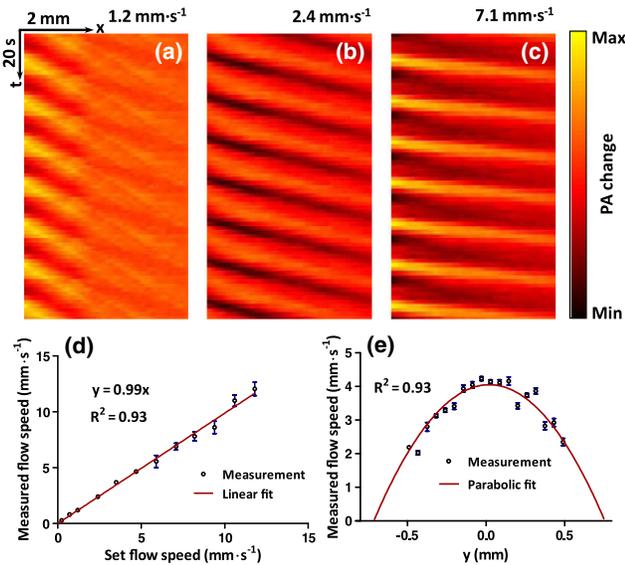
FIG. 4 (color online).   (a)–(c) Representative thermal trajectories at different blood flow speeds. (d) Measured flow speed versus set flow speed. Error bars represent standard errors. $N = 8$ for each flow speed. (e) Flow-speed distribution along the radial direction (y axis) of a cylindrical tube.

The current highest detectable flow speed is $11.8 \text{ mm} \cdot \text{s}^{-1}$, limited by the imaging frame rate and the field of view. The current 2D imaging speed is 1.6 sec/frame. Because much faster frame rates have been previously demonstrated [28], the highest detectable flow speed can be further improved.

Owing to the 2D PA imaging capability, different flow speeds can be simultaneously measured. Figure 4(e) shows the flow speed distribution across a round tube with a 1.5 mm inner diameter. A parabolic distribution in the radial direction is clearly identified. For future *in vivo* blood flow imaging, we can extract points along the curved blood vessels and then calculate the flow speed. If the flow speed changes along the vessel due to diameter change or for other reasons, then average flow speeds can be calculated in small segments. If the blood flow has strong pulsation due to beating of the heart, we can measure average flow speeds over multiple pulsation cycles. Assuming the pulsation frequency is stable and can be measured using other methods, we can set the ultrasound heating at a modulation frequency different from the pulsation. Then the pulsation will be averaged out over multiple heating cycles. Moreover, the pulsation in slow flowing vessels is not as strong as that in fast flowing vessels.

With multiple heating spots on different vessels, an even larger flow field can be simultaneously measured, and this can provide higher throughput than point-by-point flow sensing. One possible approach is to employ an ultrasound array to dynamically heat multiple spots in multiple vessels. If they are far enough apart from each other, the

contrast will not be affected. The ultrasound heating and PA detection can potentially be performed by the same transducer array to improve alignment and reduce the footprint.

Deep flow imaging was demonstrated by measuring blood flow covered with chicken breast tissue. The chicken breast, placed between the blood and the heating ultrasound transducer, diffused the PA excitation light and attenuated the ultrasound heating. As shown in Fig. 5, thermal trajectories were clearly visualized under 5 mm thickness. Since both heating and detection resolutions are acoustically defined, the spatial resolution of flow imaging scales approximately linearly with the depth. While the optical penetration depth of the imaging wavelength (800 nm) is high in biological tissue, acoustic attenuation of the heating ultrasound should be considered when imaging deeply. Lower frequency and higher power heating ultrasound transducers can be used to further extend the flow imaging depth.

During the heating, the maximum PA amplitude change was $\pm 6.2\%$. Because the PA signal depends on temperature in an approximately linear relationship, the estimated temperature fluctuation was $\pm 1.3\,^{\circ}\text{C}$ (room temperature $20\,^{\circ}\text{C}$). Such a small short-term temperature change should be safe for most *in vivo* imaging applications. The maximum temperature increase was always monitored during experiments, so that we could adjust the power of the heating ultrasound transducer to avoid overheating.

In blood flow measurement, Doppler ultrasound senses the speed of only the blood cells, not the plasma. In contrast, UE-PAF detects blood flow speed of all thermal carriers, including both plasma and blood cells, which could be different. In UE-PAF, acoustic and optical absorption, rather than scattering, provides imaging contrasts, which potentially enables label-free flow imaging of continuous absorptive media.
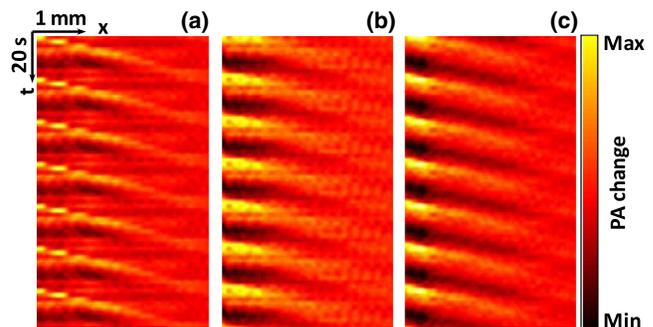

FIG. 5 (color online).   Thermal trajectories imaged beneath chicken breast tissue. (a) Without tissue, average of 7 heating cycles. (b) 3-mm-thick tissue, average of 21 heating cycles. (c) 5-mm-thick tissue, average of 35 heating cycles. The flow speed was set to $1.4 \text{ mm} \cdot \text{s}^{-1}$. The measured flow speeds for (a)–(c) were $1.5 \pm 0.1 \text{ mm} \cdot \text{s}^{-1}$, $1.6 \pm 0.2 \text{ mm} \cdot \text{s}^{-1}$, and $1.5 \pm 0.2 \text{ mm} \cdot \text{s}^{-1}$ (mean $\pm$ standard error, $N = 8$), respectively.

Conclusion.—To summarize, we present an ultrasonically encoded PA flow imaging method. A sinusoidally modulated ultrasound transducer heats the acoustically absorptive flow media and generates thermally tagged features in the fluid. PA computed tomography detects the thermal propagations in the fluid. The Doppler shift of the thermal-tagged features is employed to determine the flow speed. A blood flow speed as low as $0.24 \ \mathrm{mm \cdot s^{-1}}$ was successfully measured. Deep blood flow was clearly imaged under 5-mm-thick chicken breast tissue. Based on acoustic and optical absorption, UE-PAF has enabled high-resolution slow flow imaging in deep tissue, addressing a long-standing challenge in PA and ultrasound flow sensing. Combined with spectral imaging, UE-PAF can potentially provide simultaneous measurement of blood flow, oxygen saturation, and even the metabolic rate of oxygen, all in a single modality.

*Corresponding author.
lhwang@wustl.edu

[1] A. Benchimol, and K. B. Desser, JAMA, J. Am. Med. Assoc. **249**, 1502 (1983).

[2] E. Macé, G. Montaldo, I. Cohen, M. Baulac, M. Fink, and M. Tanter, Nat. Methods **8**, 662 (2011).

[3] K. J. Rowland, J. Yao, L. Wang, C. R. Erwin, K. I. Maslov, L. V. Wang, and B. W. Warner, Journal of pediatric surgery **47**, 1143 (2012).

[4] A. Krumholz, L. Wang, J. Yao, and L. V. Wang, J Biomed. Opt. **17**, 060502 (2012).

[5] T. H. Ting, V. L. Newhouse, and Y. Li, Ultrasonics **30**, 225 (1992).

[6] A. Heimdal and H. Torp, IEEE Trans. Ultrason. Ferroelectr. Freq. Control **44**, 873 (1997).

[7] E. Zhang, J. Laufer, and P. Beard, Appl. Opt. **47**, 561 (2008).

[8] L. Wang, K. Maslov, J. Yao, B. Rao, and L. V. Wang, Opt. Lett. **36**, 139 (2011).

[9] L. Wang, K. Maslov, W. Xing, A. Garcia-Uribe, and L. V. Wang, J Biomed. Opt. **17**, 106007 (2012).

[10] J. Yao, C. Huang, L. Wang, J. Yang, L. Gao, K. Maslov, J. Zou, and L. V. Wang, J. Biomed. Opt. **17**, 080505 (2012).

[11] L. Gao, L. Wang, C. Li, A. Garcia-Uribe, and L. V. Wang, J. Biophotonics **6**, 543 (2013).

[12] L. Gao, L. Wang, C. Li, Y. Liu, H. Ke, C. Zhang, and L. V. Wang, J Biomed. Opt. **18**, 026003 (2013).

[13] L. Wang, K. Maslov, and L. V. Wang, Proc. Natl. Acad. Sci. U.S.A. **110**, 5759 (2013).

[14] H. Fang, K. Maslov, and L. V. Wang, Phys. Rev. Lett. **99**, 184501 (2007).

[15] C.-W. Wei, S.-W. Huang, C.-R. Chris Wang, and P.-C. Li, IEEE Trans. Ultrason. Ferroelectr. Freq. Control **54**, 1131 (2007).

[16] S. Ma, S. Yang, and D. Xing, Opt. Express **18**, 9991 (2010).

[17] A. Sheinfeld, S. Gilead, and A. Eyal, Opt. Express **18**, 4212 (2010).

[18] J. Yao, K. I. Maslov, Y. Shi, L. A. Taber, and L. V. Wang, Opt. Lett. **35**, 1419 (2010).

[19] J. Brunker and P. Beard, J. Acoust. Soc. Am. **132**, 1780 (2012).

[20] A. Sheinfeld and A. Eyal, Biomed. Opt. Express **3**, 800 (2012).

[21] Z. Guo, L. Li, and L. V. Wang, Med. Phys. **36**, 4084 (2009).

[22] Z. Guo, Z. Xu, and L. V. Wang, J Biomed. Opt. **17**, 046009 (2012).

[23] See Supplemental Material at http://link.aps.org/supplemental/10.1103/PhysRevLett.111.204301 for derivation of temperature modulation amplitude, experimental setup, and blood flow video.

[24] V. L. Irina, V. L. Kirill, and O. E. Rinat, J. Phys. D **38**, 2633 (2005).

[25] J. Shah, S. Park, S. Aglyamov, T. Larson, L. Ma, K. Sokolov, K. Johnston, T. Milner, and S. Y. Emelianov, J Biomed. Opt. **13**, 034024 (2008).

[26] M. Pramanik and L. V. Wang, J Biomed. Opt. **14**, 054024 (2009).

[27] M. Xu and L. V. Wang, Phys. Rev. E **71**, 016706 (2005).

[28] R. J. Zemp, L. Song, R. Bitton, K. K. Shung, and L. V. Wang, Opt. Express **16**, 7915 (2008).